photonics

MDPI

Article

Tunable Ultra-Wideband VO_2–Graphene Hybrid Metasurface Terahertz Absorption Devices Based on Dual Regulation

Kele Chen [1,2], Zhengning Wang [1,*], Meizhang Guan [2], Shubo Cheng [3], Hongyu Ma [4], Zao Yi [4,5] and Boxun Li [6]

1 School of Information and Communication Engineering, University of Electronic Science and Technology of China, Chengdu 611731, China; chenkele1988ioe@sina.com
2 Sichuan Intronics Electronic Technology Co., Ltd., Suining 629000, China; gm794998199@163.com
3 School of Physics and Optoelectronic Engineering, Yangtze University, Jingzhou 434023, China; shubocheng@yangtzeu.edu.cn
4 Joint Laboratory for Extreme Conditions Matter Properties, Southwest University of Science and Technology, Mianyang 621010, China; 15082734560@163.com (H.M.); yizaomy@swust.edu.cn (Z.Y.)
5 School of Chemistry and Chemical Engineering, Jishou University, Jishou 416000, China
6 School of Physics and Optoelectronics, Xiangtan University, Xiangtan 411105, China; lbxcsu@xtu.edu.cn
* Correspondence: zhengning.wang@uestc.edu.cn; Tel./Fax: +86-0816-2480830

Abstract

In this study, a dynamically tunable terahertz device based on a VO_2–graphene hybrid metasurface is proposed, which realizes the dual functions of ultra-wideband absorption and efficient transmission through VO_2 phase transformation. At 345 K (metallic state), the device attains an absorption efficiency exceeding 90% (average 97.06%) in the range of 2.25–6.07 THz (bandwidth 3.82 THz), showing excellent absorption performance. At 318 K (insulated state), the device achieves 67.66–69.51% transmittance in the 0.1–2.14 THz and 7.51–10 THz bands while maintaining a broadband absorption of 3.6–5.08 THz (an average of 81.99%). Compared with traditional devices, the design breaks through the performance limitations by integrating phase change material control with 2D materials. The patterned graphene design simplifies the fabrication process. System analysis reveals that the device is polarization-insensitive and tunable via graphene Fermi energy and relaxation time. The device's excellent temperature response and wide angular stability provide a novel solution for terahertz switching, stealth technology, and sensing applications.

Keywords: phase change materials VO_2; graphene; terahertz absorber; tunable broadband

check for updates

Received: 7 August 2025
Revised: 1 October 2025
Accepted: 2 October 2025
Published: 5 October 2025

Citation: Chen, K.; Wang, Z.; Guan, M.; Cheng, S.; Ma, H.; Yi, Z.; Li, B. Tunable Ultra-Wideband VO_2–Graphene Hybrid Metasurface Terahertz Absorption Devices Based on Dual Regulation. *Photonics* **2025**, *12*, 987. https://doi.org/10.3390/photonics12100987

Copyright: © 2025 by the authors. Licensee MDPI, Basel, Switzerland. This article is an open access article distributed under the terms and conditions of the Creative Commons Attribution (CC BY) license (https://creativecommons.org/licenses/by/4.0/).

1. Introduction

In recent years, electromagnetic wave absorption technology has emerged as a cutting-edge research focus, demonstrating significant potential for applications in diverse domains, including energy conversion, environmental monitoring, and so on [1–3]. Among them, devices with broadband electromagnetic wave absorption characteristics are widely used in communications, military, medical diagnostics, and imaging fields [4–6]. In view of the depth of basic research and the potential for industrialization of this technology, the global scientific research team is continuously improving its performance indicators through various strategies, such as structural design innovation and material system optimization. At present, related research has given rise to a variety of new types of devices. According to bandwidth, these can be divided into wide/narrowband absorbers [7–9]. According to the response frequency band, they can be divided into single-frequency/multi-frequency absorbers [10,11]. According to configuration differences, metasurface absorbers and

dynamically tunable absorbers are covered, and these breakthroughs have provided a solid basis for the advancement of electromagnetic wave absorption technology [12,13].

Among many functional materials, vanadium dioxide (VO_2), a phase change material, offers a novel approach to designing broadband absorbers due to its unique dynamic control characteristics [14,15]. As a typical strongly correlated phase change material, VO_2 has garnered significant interest in smart materials owing to its unique metal–insulator transition (MIT) characteristics [16,17]. When the temperature reaches a critical point (about 68 °C), VO_2 undergoes a reversible structural transition from monoclinic to tetragonal, accompanied by a sudden change in conductivity of up to five orders of magnitude (from 10^2 S/m to 10^5 S/m). This phase change process has significant thermal hysteresis properties—the transition starts at 340 K when heated and 334 K when cooled, with a temperature difference window of 6 K, ensuring stable material properties [18]. Even more strikingly, this phase transition can be completed in picoseconds, making it an ideal material for the development of highly sensitive terahertz devices [19,20]. Through multi-physics manipulation of optical, electrical, and thermal fields, VO_2 can achieve precise switching between the metallic state and the insulating state, and this dynamic tunability provides a novel approach to designing new intelligent devices, such as reconfigurable metamaterials and adaptive thermal control coatings [21,22].

Moreover, graphene materials also play a significant role in electromagnetic absorption. As a special form of carbon, graphene is unique in materials research with its unique single-atomic-layer two-dimensional structure [23–25]. This sp^2-bonded 2D material with a hexagonal honeycomb structure typically has a sheet size between 10 and 100 nanometers, and this microstructure characteristic allows it to exhibit excellent electromagnetic wave absorption characteristics in the mid-infrared to terahertz frequency band [26,27]. Compared with conventional functional materials, the material not only has excellent environmental stability and carrier migration characteristics but also exhibits excellent mechanical strength and electrical and thermal conductivity. It is particularly noteworthy that the unique properties of the Fermi level are controlled by external bias voltage, so electromagnetic wave absorption modulation devices based on this material can achieve dynamically adjustable absorption characteristics [28,29]. Notably, the combination of graphene and phase change VO_2 represents a relatively novel design paradigm in current terahertz absorber research. For instance, Shen et al. proposed a VO_2–graphene hybrid metamaterial absorber with excellent overall absorption performance, yet its seven-layered structure leads to high fabrication complexity, leaving room for structural optimization [30]. Complementing the phase transition control of VO_2, graphene provides another option for absorber design. Although there are still technical bottlenecks in the large-scale preparation and cost control of graphene, with the continuous optimization of the preparation process, this revolutionary material is moving from the laboratory to industrial application [31,32].

In this study, we combine graphene with the phase change material VO_2 to develop a new type of ultra-wideband response phase change device. The device consists of a classic three-layer thin film structure, with specially patterned graphene on the top, which is composed of several simple rectangular shapes. SiO_2 is employed as the dielectric layer and VO_2 as the substrate of the device. At the relatively high temperature of T = 345 K, VO_2 displays a metallic state, and this device shows perfect ultra-wideband absorption of terahertz bands, with an absorption efficiency of more than 90% in the frequency range of 2.25 THz–6.07 THz and a total of 3.82 THz, demonstrating an averaged absorption of 97.06%. At the relatively low temperature of T = 318 K, VO_2 exhibits a dielectric state, and this device demonstrates broadband absorption across the frequency band of 3.6 THz–5.08 THz, with an average absorption rate of 81.99%. At the same time, the device also exhibits good transmission ability at relatively low temperatures, exhibiting a mean transmittance of

67.66% and 69.51% across the frequency bands of 0.1–2.14 THz and 7.5–10 THz, respectively. First, we describe the fabrication process of the device, which is made easier to fabricate by using simple patterned graphene. Second, the phase transition mechanism of VO_2 is explained in detail, and the performance transition caused by this change is explored. Subsequently, we investigate the relative impedance matching and the interfacial E-field in the device at relatively high temperatures, analyze the absorption mechanism, and confirm the polarization-independent behavior of the device. On this basis, the effects of the chemical parameters of graphene, such as the Fermi energy level, relaxation time, and important physical parameters of the device's impact on absorption performance, are analyzed. At the end of the article, we analyze the effects of different polarizations and angles of incidence on the absorption performance of the device. Compared with previous articles, this study demonstrates that the device has excellent characteristics, such as high absorption and transmission efficiency, bias manufacturing, and phase change control, and it is believed that the device can shine in the fields of terahertz communication, terahertz switching, terahertz stealth, and medical detection.

2. Numerical Model and Structural Design

The proposed ultra-wideband phase change device is presented in Figure 1. Figure 1a shows a cell-level layout diagram of the ultra-wideband phase change device, which consists of a fundamental three-component thin film structure. As shown in Figure 1b, the topmost layer is a patterned 1 nm graphene layer composed of three simple rectangular graphene layers. The middle dielectric layer of the device is SiO_2, and the relevant dielectric parameter data comes from Kitamura [33]. The substrate layer of the device is VO_2, and the relevant dielectric constant is from reference [14]. The device exhibits excellent absorption and transmission characteristics at 0.1–10 THz. See Table 1 for the specific device parameters.

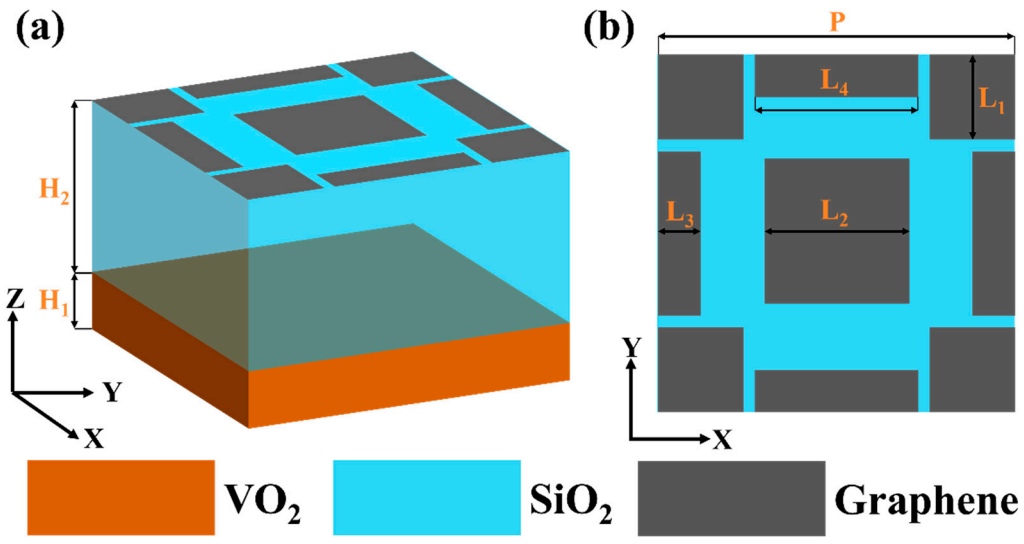

Figure 1. (**a**) A cell-level layout diagram of the ultra-wideband phase change device. (**b**) XY plane top view of the device.

Table 1. Parameters of an ultra-wideband phase change device.

Parameter	L1	L2	L3	L4	P	H1	H2
Value (μm)	5	8.5	2.5	9.6	21	5	12

As shown in Figure 2, we demonstrate a simple and feasible process for fabricating this ultra-wideband phase change device. Firstly, the VO_X film was deposited on the substrate by magnetron sputtering, and the VO_2 layer was formed by annealing in an O_2 atmosphere. A 12-micron-thick SiO_2 dielectric layer was then deposited by magnetron sputtering. Graphene sheets were prepared independently using CVD technology, the desired pattern was formed by electron beam lithography, and finally, the patterned graphene was transferred to the SiO_2 surface to complete the device fabrication [34,35].

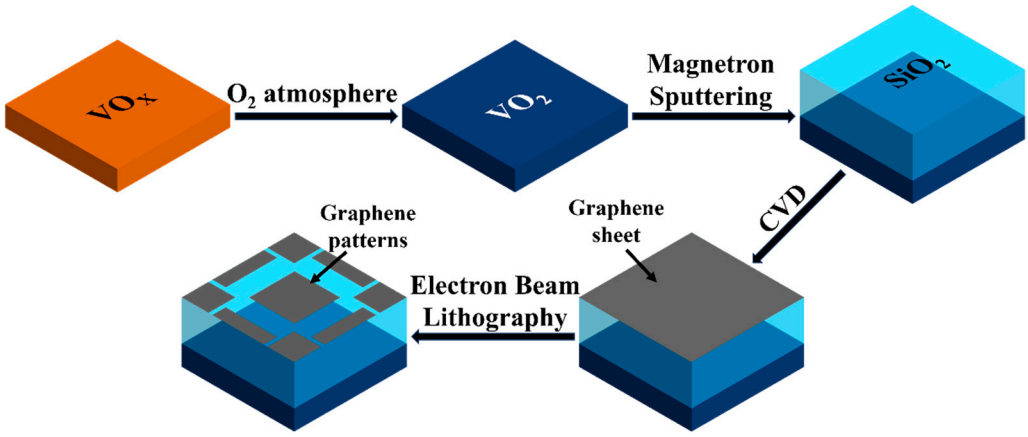

Figure 2. Simple layout representation of the fabrication process of the ultra-wideband phase change device.

After constructing the basic model structure diagram, we used CST simulation software to simulate the electromagnetic behavior of the model and used the FDID algorithm to simulate the model [36,37]. First, periodic boundary conditions were applied along the X and Y axes, while the *Z*-axis remained open, along which the electromagnetic wave travels in the negative *Z*-axis direction [38]. Based on this design, we were able to simulate and calculate the entire periodic array using only a single device unit, as shown in Figure 1a, which greatly reduces the time required for calculation and speeds up the research while maintaining the computational precision. In addition, we used the S-parameter inversion method to represent the reflectance (R) and transmittance (T) of the device, respectively; thus, the absorption rate (A) can be easily obtained, demonstrating the device's capability, and the specific formula is as follows [39,40]:

$$A(\omega) = 1 - R(\omega) - T(\omega) = 1 - |S_{11}|^2 - |S_{21}|^2 \quad (1)$$

In the above formula, $T(\omega)$ and $R(\omega)$ are the transmittance and reflectivity of the impinging optical wave when irradiating the structure of the absorbing unit, respectively, ω is the angular frequency, and $|S_{11}|^2$ and $|S_{21}|^2$ indicate the reflection and transmission coefficients, respectively.

In addition, we used the Drude model to represent the surface conductivity of the graphene layer used in the ultra-wideband phase change device during the simulation, as follows [14,41]:

$$\sigma(\omega) = \frac{e^2 E_F}{\pi h^2} \frac{i}{\omega + i\tau^{-1}} \quad (2)$$

In Equation (2), where ω and h denote the incident wave frequency and reduced Planck constant, respectively, defining E_F as the Fermi level and τ the relaxation time in graphene, these two parameters are as follows [42]:

$$E_F = V_F \sqrt{\frac{\pi \varepsilon_0 \varepsilon_\gamma V_0}{e_0 n_s}} \tag{3}$$

$$\tau = \frac{\mu E_F}{e_0 V_i^2} \tag{4}$$

In Equation (3), V_0 represents the magnitude of the external voltage, e_0 refers to the number of electron charges, V_F represents the Fermi velocity, and n_s is used to represent the number of layers of SiO_2 in the structure. In Equation (4), $\mu = 10^4$ cm^2/(V.S) represents the carrier mobility, $V_i = 10^6$ m/s is the aforementioned Fermi velocity, and E_F is the Fermi level in Equation (3). Based on this, we can easily come up with the corresponding dielectric constant formula [43]:

$$\varepsilon = 1 + \frac{i\sigma(\omega)}{\varepsilon_0 t \omega} \tag{5}$$

In Equation (5), ε_0 represents the conductivity in a vacuum environment and t denotes the graphene layer's thickness. The graphene used in this paper has a thickness of 1 nm, a relaxation time of 0.1 ps, and a Fermi level of 1.0 ev.

After the construction of graphene materials was completed, we also employed the Drude model to establish VO_2 materials in the terahertz band, and the relevant formulas are as follows [14,44]:

$$\varepsilon(\omega)_{VO_2} = \varepsilon_\infty - \frac{\omega_p^2}{\omega(\omega + i\gamma)} = \varepsilon_\infty - \frac{\sigma \omega_{p_0}^2}{\sigma_0 \omega(\omega + i\gamma)} \tag{6}$$

where ε_∞ is used to express the dielectric constant at high frequencies with a value of 12. γ is the collision frequency; the value is 5.75×10^{13} rad/s. ω_p is the plasma frequency, $\omega_{p_0}^2$ is 1.4×10^{15} rad/s, and the σ_0 value is 3×10^5 s/m. Based on the above data, we obtained the relationship between the conductivity of VO_2 and the permittivity using Equation (6) above. In the simulation software, we can represent VO_2 at different temperatures by changing the conductivity of VO_2, and the related temperature and state relationship is shown in Figure 3. As the temperature increases from 318 K to 345 K, the dielectric-to-metal transition occurs in VO_2 due to its phase transformation properties, with the corresponding thermal and dielectric property curves during heating/cooling shown in Figure 3a.

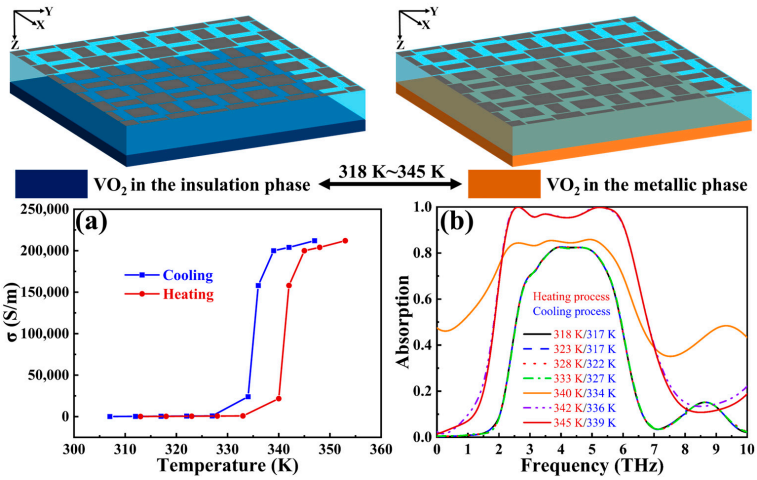

Figure 3. Vanadium dioxide undergoes phase transformation during a temperature change from 318 K to 345 K. (**a**) The conductivity variations with temperature are plotted as curves for VO_2 film under heating and cooling. (**b**) Variation of the absorption spectrum (unitless) of the ultra-wideband phase change device at different temperatures under heating and cooling.

3. Parameter Calculation and Result Analysis

After the above analysis and simulation process was completed, we calculated the absorption efficiency of the ultra-wideband phase change device in the cooling (317–339 K) and heating (318–345 K) states, respectively, and plotted the absorption spectrum of the device under the corresponding conditions, as illustrated in Figure 3b. The data in the figure illustrates that when heated to 342–345 K, VO_2 transitions to the metallic phase, and the device exhibits ultra-wideband perfect absorption in the terahertz band, with absorption efficiency exceeding 99% at a specific frequency point. In the relatively low temperature range of T = 318–333 K, VO_2 shows an insulating phase, and the device still maintains excellent broadband absorption, exhibiting an average absorption rate of 81.99%. It is worth noting that the cooling and heating processes exhibit a thermal hysteresis effect of 6 K, but the overall variation law is basically the same. These results fully show that the device has temperature control characteristics, and the absorption of the device in the terahertz band exhibits temperature-dependent characteristics, and the absorption efficiency can be changed from 0 to 99% over a wide range.

The thermal modulation of absorption was quantified through temperature-dependent spectra at 345 K (Figure 4a), highlighting the device's optothermal response. At 345 K, the device produces an ultra-wideband absorption of more than 90% spanning 2.25–6.07 THz and a total of 3.82 THz, averaging 97.06% absorption in this band. The absorption spectrum fluctuates three times in this range, and the device exhibits perfect absorption of 99.93% at P1 = 2.62 THz, 96.88% at P2 = 3.49 THz, and 99.85% at P3 = 5.24 THz. In addition, we used TE and TM waves to act on the device, respectively, and the absorption efficiency curve remained almost unchanged, which shows the polarization insensitivity of the device [45,46].

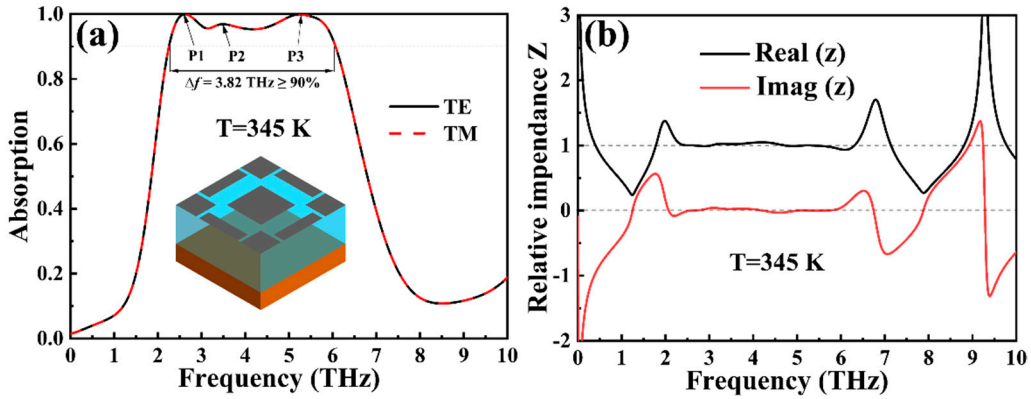

Figure 4. (**a**) TE/TM-polarized light absorption (unitless) in an ultra-wideband phase change device across 0.1–10 THz and 345 K. (**b**) Relative impedance diagram of the device in the same case.

To investigate the absorption mechanism in depth and validate the reliability of our computational findings, we introduce the effective impedance matching theory to invert the obtained absorption data, and the relevant formulas of the impedance matching theory are as follows [47,48]:

$$Z = \pm\sqrt{\frac{(1+S_{11})^2 - S_{21}^2}{(1-S_{11})^2 - S_{21}^2}} \tag{7}$$

In Equation (7), S_{11} and S_{21} indicate the reflection and transmission coefficients, respectively. For the impedance matching analysis, when the imaginary part of the impedance Imag (z) is close to 0 and the real part of the impedance Real (z) is close to 1, it is considered that the impedance of the ultra-wideband phase change device is perfectly matched with the spatial impedance, which also corresponds to the generation of perfect absorp-

tion [49,50]. In Figure 4b, we have plotted the relative impedance of the device, and it is obvious that the impedance matching plot in the band of 2.25–6.07 THz is the same as the theoretical effect, which not only explains why the device can produce an excellent effect, demonstrating >97% average absorption in this frequency band, but also verifies that our calculation results accurately match the relative impedance matching theory.

Subsequently, we numerically simulated and visualized the device's surface E-field distribution, as illustrated in Figure 5. First, we regionally number the top-layer graphene of the ultra-wideband phase change device, which provides a clear reference framework for the subsequent analysis of the E-field distribution characteristics of the surface, as illustrated in Figure 5a. The constructive superposition mechanism of different resonant modes originates from the spatial distribution decoupling and frequency-domain response complementarity. In the low-frequency band of P1 = 2.62 THz, a symmetric dipole resonance is formed at the edge of graphene (such as the periphery of block 3), with the electric field showing a symmetric distribution. In the middle-frequency band of P2 = 3.49 THz, the nanogap between block 1 and block 3 excites localized surface plasmon resonance (LSPR), capturing electromagnetic energy at the subwavelength scale through near-field coupling [51,52]. In the high-frequency band of P3 = 5.24 THz, it is characterized by cross-unit multipolar resonance coupling, with reverse electric field oscillations formed at the center of block 2 and the edges of block 1/3. As the frequency increases from P1 to P3, the electric field distribution gradually shifts from the single-block edge to the double-block gap and cross-unit region, avoiding phase cancellation caused by spatial overlap. In terms of the frequency domain, the half-widths of the three are 1.2 THz, 1.5 THz, and 1.1 THz, respectively, the frequency band overlap rate exceeds 60%, the real part of the impedance in each frequency band is close to 1, and the imaginary part is approximately 0 (as shown in Figure 4b), meeting the wide-frequency impedance matching condition and finally achieving continuous and efficient absorption at 3.82 THz. The E-field distributions corresponding to the three characteristic absorption peaks P1 = 2.62 THz, P2 = 3.49 THz, and P3 = 5.24 THz are shown in Figure 5b–d, respectively. At the low-frequency absorption peak P1 = 2.62 THz (Figure 5b), the E-field is mainly localized at the peripheral edge of block 3 (the maximum field strength is about 4×10^6 V/m), showing a symmetrically distributed dipole resonance pattern. When the frequency is increased to P2 = 3.49 THz (Figure 5c), the concentrated region of the E-field shifts to the nanogap between blocks 1 and 3, and the field strength is significantly enhanced to 5×10^6 V/m, which is due to the local surface plasmon resonance (LSPR) excited at the gap, and the electromagnetic energy is efficiently captured at the subwavelength scale through near-field coupling [53,54]. When the frequency is further increased to P3 = 5.24 THz (Figure 5d), the E-field distribution shows the characteristics of multi-region synergistic resonance. The longitudinal edge of the central region of block 2 has a strong field area, and the edges of block 1 and block 3 form an inverted oscillation, which is also concentrated in the longitudinal gap between block 1 and block 3 and maintains the maximum field strength. This multipole resonance coupling across cells effectively extends the absorption bandwidth of the device [55]. It is worth noting that the geometric arrangement of blocks 1 and 3 in the graphene layer and the central region 2 forms a cascading resonance structure. As the incident wave frequency shifts from P1 to P3, the local position of the E-field changes from single block edge (P1) to double block gap (P2) and cross-cell multi-region (P3), and this controlled tuning of the spatial distribution enables the device to achieve ultra-wideband absorption spanning 2.25–6.07 THz. The gradient of E-field intensity (0–5×10^6 V/m) shown in the chroma bar on the right further confirms the local enhancement effect of nanostructures on electromagnetic fields.

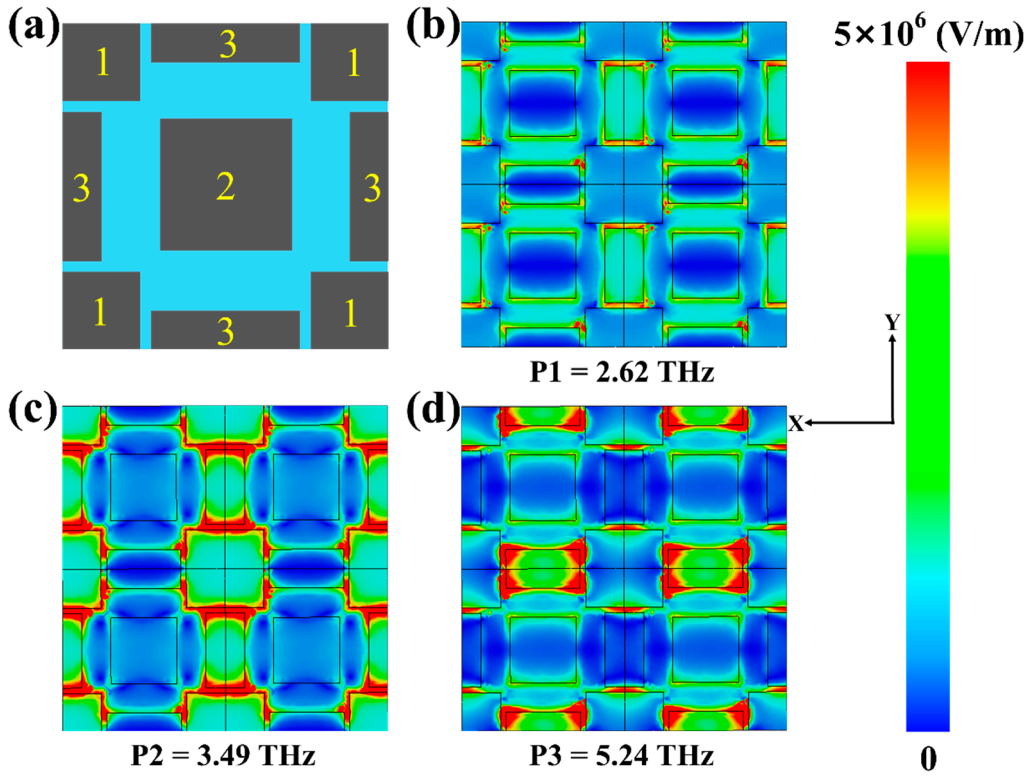

Figure 5. (**a**) Convenient numbering of graphene in the top layer of an ultra-wideband phase change device. (**b**–**d**) XY surface E-field distribution of the three absorption peaks at P1 = 2.62 THz, P2 = 3.49 THz, and P3 = 5.24 THz at T = 345 K.

As shown in Figure 6, to investigate the influence of the top-layer graphene structure on the terahertz band absorption efficiency of the device, we designed comparative experiments with different structures and tested their absorption performance. The red curve in the figure corresponds to the absorption characteristics of the "three-rectangle patterned graphene" structure proposed in this paper (Figure 1b). The absorption mechanism and performance advantages of this structure have been detailed in the above text (e.g., Section 3, "Parameter Calculation and Result Analysis", and the E-field distribution analysis in Figure 5) and will not be repeated here. It can be seen from the curve that the absorption effect of this structure in the target frequency band is significantly better than that of other comparative structures. Regarding the other three comparative curves, the blue curve corresponds to the structure with "the central block 2 of the top-layer graphene removed". In the 2.25–6.07 THz band, its average absorption rate is 88.91%. Although it maintains good absorption performance, it is 8.15 percentage points lower than that of the red curve. The green curve corresponds to the structure with "the surrounding block 3s of the top-layer graphene removed". In the 2.25–6.07 THz band, its average absorption rate is 85.57%, and the absorption rate in the 2.91–5.18 THz band can exceed 90%, still exhibiting a certain broadband absorption capability. However, its overall absorption efficiency is 11.49 percentage points lower than that of the red curve. The black curve corresponds to the device with "the top-layer graphene replaced by a full-coverage unpatterned structure". For this structure, the absorption efficiency decreases significantly in the 2.25–6.07 THz band, with an average absorption rate of less than 80% and no obvious high-absorption frequency band. Its overall performance is poor and has no discussion value. In conclusion, by comparing the absorption performance of different top-layer graphene structures, it can be concluded that the "three-rectangle patterned graphene" structure proposed in this paper achieves the optimal absorption effect in the terahertz band. The resonant modes

(edge dipole resonance, gap LSPR, and cross-unit multipolar resonance) synergistically excited by its multi-rectangle units are key to realizing ultra-wideband and high-efficiency absorption, which further verifies the rationality and necessity of this structural design.

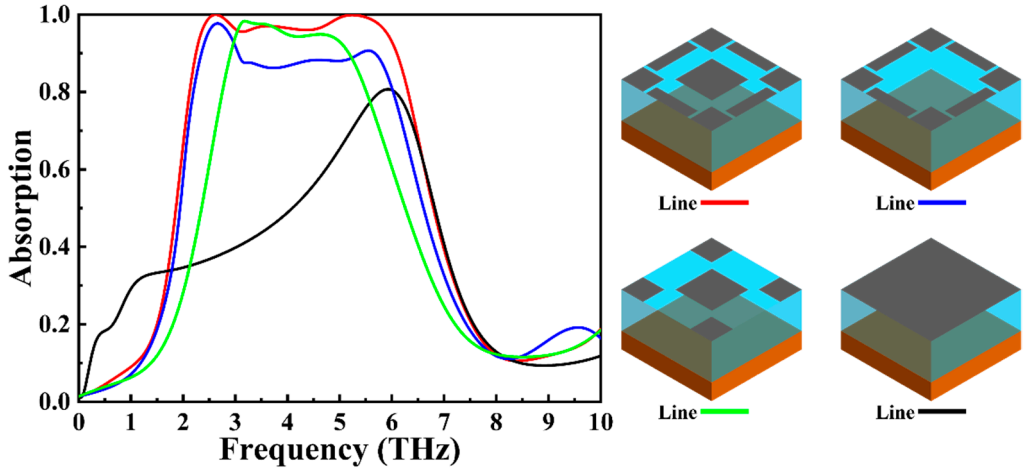

Figure 6. Comparison of absorption spectra of different graphene structures (T = 345 K).

After the study of the device at a relatively high temperature, the absorption spectra of the device at a relatively low temperature of T = 318 K were plotted and analyzed separately, as shown in Figure 7. Figure 7a also shows the absorption spectrum of the device in the frequency band of 0.1–10 THz under this temperature state, and the experimental data indicate that the device still maintains the broadband absorption characteristics after changing the temperature, and the absorption efficiency exceeds 80% over 1.48 THz between 3.60 and 5.08 THz, and the average absorption rate in this range is 81.99%. TE waves and TM waves were also used to act on the device, and nearly consistent absorption spectra were obtained, which once again proves that the polarization insensitivity of the device is differentiated [56]. Combined with Equation (7) above, we analyzed the impedance matching of the device at 318 K, as illustrated in Figure 7b. Obviously, the device still conforms to the relative impedance matching theory at this time, which proves that our device is consistent with classical physics theories regardless of whether it is in a high or low temperature state, and it also shows that the results of our simulation are accurate [57]. In addition, we calculated and plotted the transmission spectrum of the device at low temperatures, as shown in Figure 7c. It can be seen from the figure that the device has dual-frequency transmission performance at low temperatures, with an average transmittance of 67.66% at 0.1–2.14 THz and 69.51% at 7.51–10 THz. In summary, the device still conforms to the impedance matching theory at low temperatures, is not polarization sensitive, and has good broadband absorption and ultra-wideband transmission characteristics, which further proves that the device can be controlled by temperature, indicating the advantages.

Based on the above research, we investigated the impact of fundamental device parameters on overall absorption performance to explore control methods beyond temperature tuning. As shown in Figure 8, we first analyzed the effect of graphene's top-layer Fermi level on absorption at 345 K. Notably, we can modulate the Fermi level of graphene by applying an external bias voltage, as described in Equation (3). Figure 8 presents a parametric sweep clearly reflecting absorption efficiency changes with EF. At T = 345 K (Figure 8a), increasing the Fermi level from 0.6 eV to 1.0 eV progressively enhances absorption. In the 2.25–6.07 THz band, the average absorption rises from 85.10% (0.6 eV) to 97.06% (1.0 eV), stabilizing at ~97% for higher E_F. This trend aligns with the linear dispersion relation in graphene's electronic band structure, where a higher E_F increases conduction electron density near the Dirac point, strengthening Drude-like free-carrier absorption of terahertz

waves [58–60]. Additionally, elevated electron density modifies the graphene metasurface's plasmonic resonance, optimizing impedance matching with VO_2 and extending the absorption bandwidth.

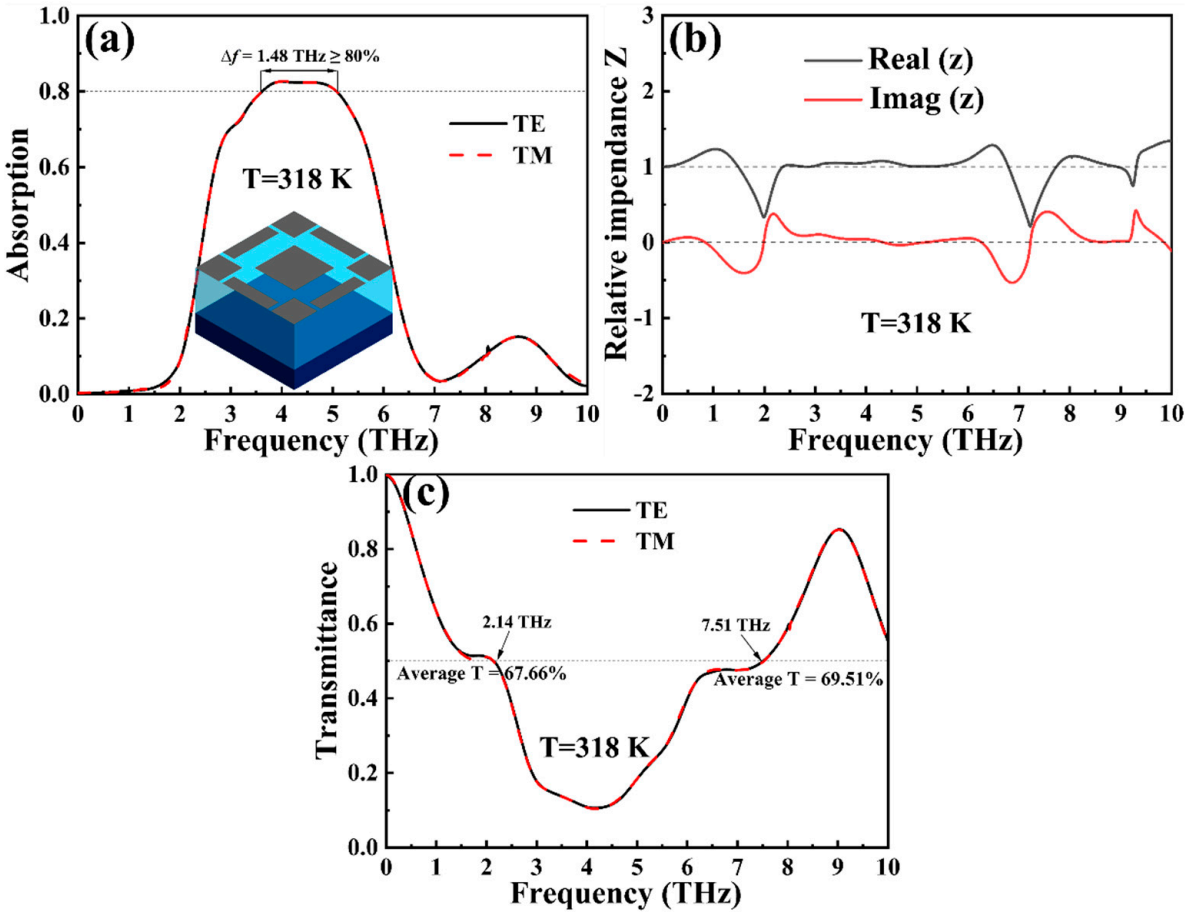

Figure 7. (**a**) TE and TM absorption spectra (unitless) of an ultra-wideband phase change device at 0.1–10 THz and T = 318 K. (**b**) Relative impedance diagram of the device in the same case. (**c**) TE/TM transmission spectra of ultra-wideband phase change devices.

After exploring the graphene Fermi level, we immediately began to explore the time of relaxation for graphene. As shown in Figure 8b, we plotted the spectrum of the absorption efficiency of a device with an increase in the time of relaxation for graphene from 0.1 ps to 0.9 ps, and the related formula for the relaxation time of graphene is shown in Equation (4) above. It is evident from Figure 8b that when the time of relaxation for graphene is 0.1 ps, the overall broadband absorption effect is the best. As the relaxation time increases, the broadband absorption effect gradually deteriorates, and the overall narrowband absorption trend is presented. This could be attributed to the extension of the relaxation time, which speeds up the energy dissipation rate within the material, resulting in the deterioration of the broadband absorption effect, which results in a narrow-band absorption peak with good absorption [61]. The alteration of relaxation time has a tendency to narrow the absorption bandwidth, which may provide some inspiration and reference for future research and will not be further studied in this paper. It has basically the same effect at low temperatures and will not be explored here.

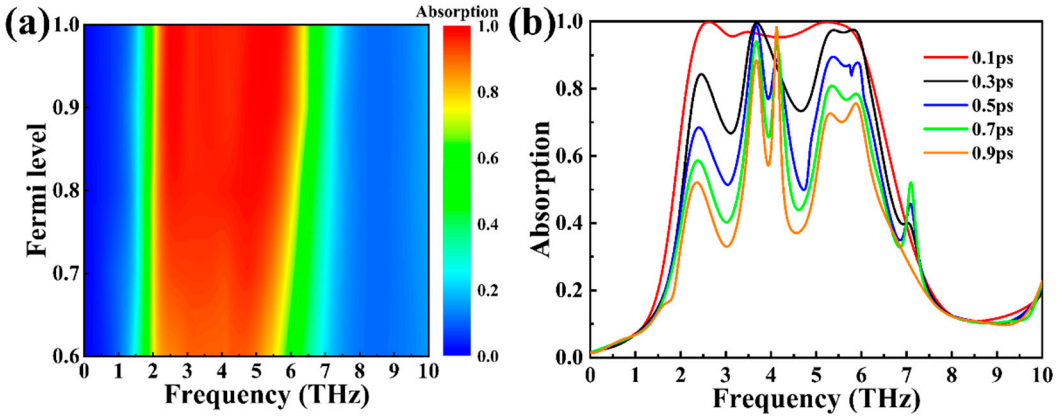

Figure 8. (**a**) Effect of different graphene Fermi levels on top of the ultra-wideband phase change device at T = 345 K. (**b**) Effect of different relaxation times of graphene on the absorption efficiency (unitless) of the device at a temperature of 345 K.

Continuing to investigate the effects of changes in the physical parameters of the device, as shown in Figures 9 and 10, we explored the influence of changes in the physical parameters of the device on the absorption efficiency, as presented in Table 1 above. Figure 9 plots the spectral curves corresponding to the parameter changes of the four graphene sheets L1–L4. As illustrated in Figure 9a, we change the L1 parameter from 4.6 to 5.4 μm, and the absorption of the device shows a certain degree of redshift. In the same way, the average absorption rates of the device in the 2.25–6.07 THz band proposed above for L1 of 4.6, 4.8, 5.0, 5.2, and 5.4 μm were 96.21%, 96.94%, 97.06%, 96.68%, and 94.98%, respectively, and the average absorption rate reached the maximum value at L1 = 5.0 μm. At the same time, the change of L1 mainly affected the absorption effect of the characteristic absorption peak P1, and there was little change between P2 and P3. Figure 9b shows the change in absorption efficiency of L2 from 7.5 μm to 9.5 μm. Since the change in L2 has a slight influence on the change in the overall absorption efficiency of the piece, we drew the contour plot after the scanning parameters to demonstrate the consistency of the absorption rate more intuitively. We selected a median of 8.5 μm as the specific parameter of L2, and the effect of L2 on the absorption efficiency demonstrates that the device can tolerate a certain manufacturing error on the L2 parameter in the manufacturing process, and an error in the range of 2 μm will not have much impact on the overall absorption effect of the device [62]. The L3 parameters are shown in Figure 9c. For the same frequency band, when L3 is 1.5 μm, 2.0 μm, 2.5 μm, 3.0 μm, and 3.5 μm, the corresponding average absorption rates are 92.52%, 95.50%, 97.06%, 95.84%, and 92.56%, respectively. The average absorption first rises and then decreases, and when the L3 value is 2.5 μm, the average absorption effect is the best, and the absorption influence of the characteristic absorption peaks P2 and P3 is also the best. Figure 9d shows the change in parameter L4, which is similar to that of (b). Changing this parameter within this range has little effect on the absorption efficiency of the device, and it is believed that similar conclusions can be drawn. When the L4 parameters are 9.2, 9.4, 9.6, 9.8, and 10.0 μm, the absorption rates corresponding to P1 are 99.26%, 99.91%, 99.93%, 99.63%, and 97.87%, respectively, and the rate of absorption attains the maximum value when the L4 parameter is 9.6 μm, so we believe that 9.6 μm should be the optimal parameter for L4. Summarizing the analysis of the impact of alterations in the four parameters of the graphene layers, we prove that the four graphene layer size parameters given in Table 1 of this article are the optimal values after our calculation and discussion, and changes in these four parameters within the range we discuss have no great impact on the overall device of the device, which can basically maintain the mean absorption rate of the device in the explored terahertz band above 95%, and it can also be

said that Figure 9 provides some references for the acceptable error range in the device manufacturing process.

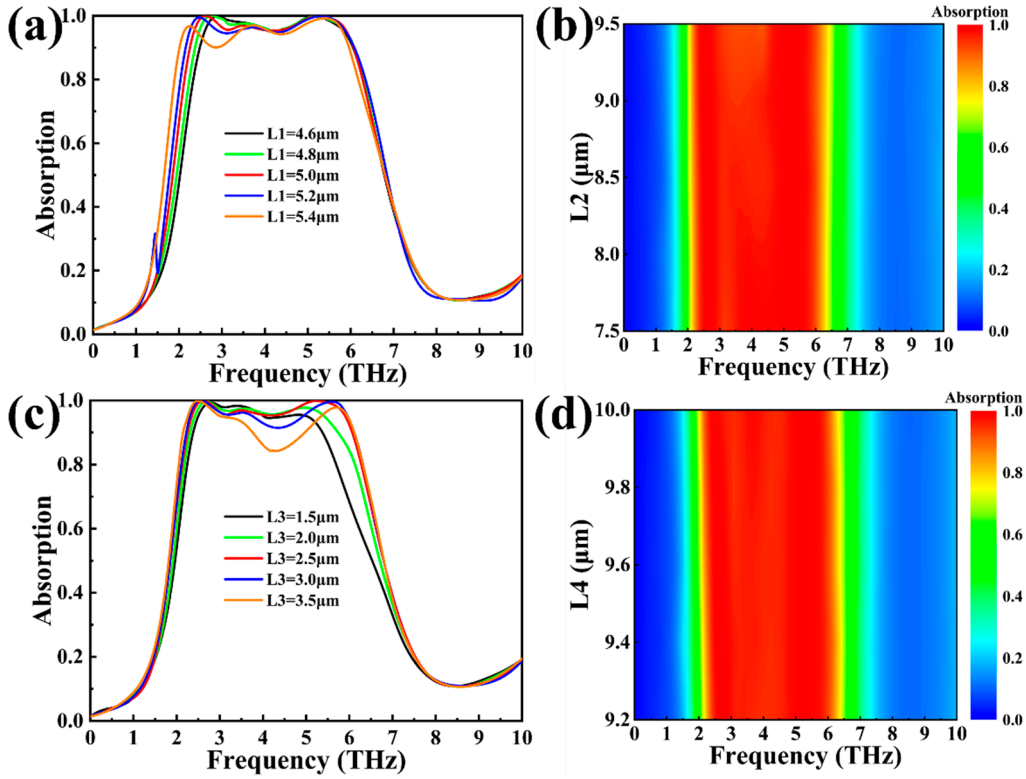

Figure 9. Influence of structural parameters of top-layer graphene on the absorption efficiency (unitless) of ultra-wideband phase change devices at T = 345 K. Each subfigure shows the influence of different parameter variations: (**a**) L1; (**b**) L2; (**c**) L3; (**d**) L4.

To further improve the device parameters, as shown in Figure 10, after exploring L1–L4, we studied the effect of changing the H1, H2, and P parameters on the absorption rate of the device. Figure 10a shows the corresponding results for the variation of H1. It can be observed that the device's absorption performance remains almost unchanged with the variation of H1. This is primarily because when T = 345 K, VO_2 is in the metallic phase, serving as a metallic substrate for the device. The thickness of VO_2 (H1 = 5 μm) is significantly greater than the skin depth in this frequency band. Specifically, at 3 THz, the skin depth of VO_2 in the metallic phase is approximately 20 nm, while the thickness of H1 is 5 μm (5000 nm), which is 250 times larger than the skin depth. This allows VO_2 to fully reflect the incident terahertz waves, enabling the absorption layer to reabsorb the reflected waves for perfect absorption, with VO_2 itself having almost no impact on the absorption performance. Figure 10b shows the correlation of changes in H2. As can be seen in the figure, when the H2 layer gradually increases, the high-frequency part of the absorption curve has a more obvious redshift, which may be due to the fact that the high-frequency terahertz wave reflected back to the absorption layer by the substrate is partially consumed in the dielectric layer when its thickness has increased, so the relative overall bandwidth becomes smaller [63,64]. When H2 is 10, 11, 12, 13, and 14 μm, the average absorption rates in the band range of 2.25–6.07 THz are 91.98%, 95.30%, 97.06%, 95.63%, and 91.53%, respectively, and the mean absorption rate reaches a peak when the H2 value is 12 μm. Finally, we explored the corresponding effect of the P size of the device cycle, as shown in Figure 10c. When P is 21, 22, 23, 24, and 25 μm, the mean absorption efficiency of the device in the discussed frequency band is 97.06%, 93.78%, 92.70%, 91.32%, and 88.86%, respectively, showing a downward trend, and when P is 21 μm, that is, the size of the

SiO_2 dielectric layer and the VO_2 substrate is just the size of the top layer of graphene, the device's absorption effectiveness is the best.

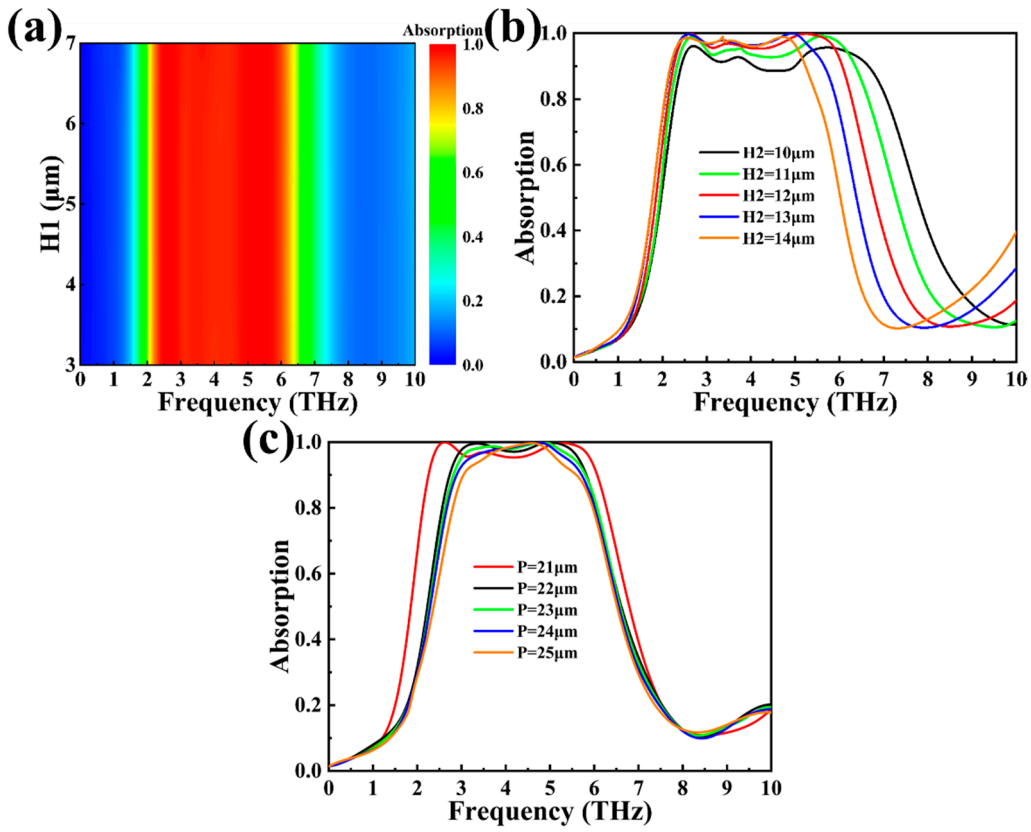

Figure 10. Influence of structural parameters of an ultra-wideband phase change device on absorption efficiency (unitless) at a temperature of 345 K. (**a**) Parameter scan of the effect of H1 on the efficiency of absorption. (**b**) Spectral pattern of the effect of H2 on absorption efficiency. (**c**) Spectral diagram of the effect of P on the efficiency of absorption.

In addition to temperature and device parameters, changes in the polarization angle and incidence angle of light are also important indicators for evaluating devices. In actual applications, the incidence angle of electromagnetic waves may not be perpendicular to the incidence angle of the device, and a device that can adapt to multiple incidence angles is suitable for more application scenarios [65–67]. As shown in Figure 11, we plotted the contour plot of the impact of angle of polarization and angle of incidence changes on the absorption efficiency of the apparatus when the temperature is 345 K. Figure 11a shows the spectrum of the absorption efficiency of the device for polarization angles of 0 degrees to 90 degrees, and it is clearly apparent that the absorption of the device is not influenced by the polarization angle, because the device we designed is a center-symmetrical structure, and the change of polarization angle will not change the plane wave received by the absorbing layer, so the device is polarization insensitive [68–72]. Figure 11b is a scan of the absorption spectrum of the device with a change of incidence angle of 0–80 degrees, and it is obvious that when the incidence angle increases from 0 to 50 degrees, the absorption remains basically unchanged, and the average absorption rate is maintained at 90% or more. When the angle is greater than 50, more than 90% of the absorption frequency band is split from about 4.5 THz, and the angle gradually increases from 50 degrees to 70 degrees, and the low frequency band and high frequency band can still maintain a relatively good absorption trend, but the absorption of the high frequency band continues to move to the higher frequency band with the change of angle, and the high absorption bandwidth

of the low frequency band gradually decreases. When the incidence angle increases to 80 degrees, the high absorption frequency band of the device is mainly displayed in the high frequency band, and the overall absorption effect becomes worse, mainly because the incidence angle is too large, so only a small part of the electromagnetic wave can irradiate the surface of the device, and we believe that an incidence angle greater than or equal to 80 degrees is too extreme to warrant continuing the discussion. In general, the ultra-wideband phase change device is impervious to the alteration of the polarization angle and can adapt to a wide range of changes in the incidence angle from 0 to 60 degrees (the average absorption efficiency is maintained at 80% and above), which is suitable for a variety of application scenarios [73–75].

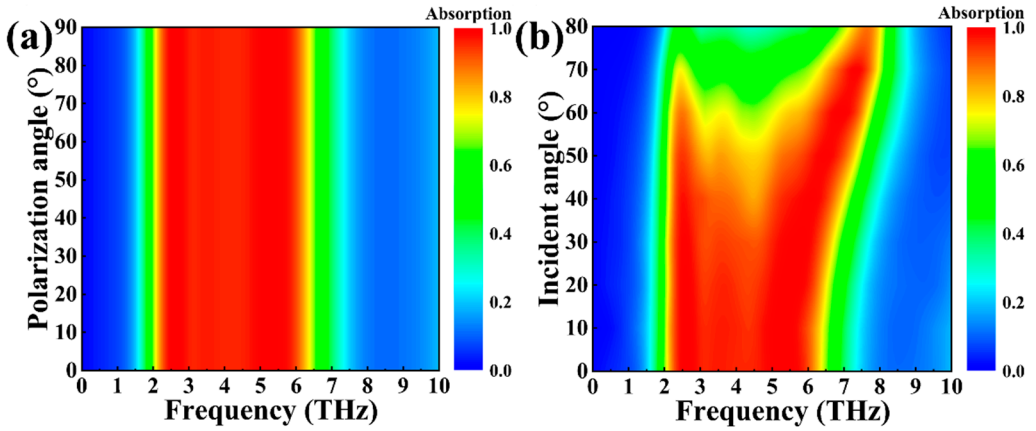

Figure 11. (**a**) Scans of absorption efficiency (unitless) at different polarization angles at a temperature of 345 K. (**b**) Scans of absorption at different angles of incidence at T = 345 K.

To conclude the article, we compare the performance of this ultra-wideband phase change device with the other studies, as shown in Table 2 [30,76–79]. The combination of phase change material VO_2 and graphene enables the absorption device to have better performance and more flexible control methods.

Table 2. Comparison of the performance of this ultra-wideband phase change device with other devices.

Ref.	Materials Used	Number of Device Layers	Absorption Range (>90%)	Bandwidth (>90%)	Average Absorption	Angle of Incidence
[76]	Graphene	5	0.82–1.87 THz	1.05 THz	Over 90%	0–60°
[77]	Graphene	3	3.29–5.25 THz	1.96 THz	Over 90%	0–60°
[78]	VO_2	5	2.37–4.56 THz	2.19 THz	Over 90%	0–55°
[30]	VO_2–Graphene	7	2.42–4.83 THz	2.41 THz	Over 90%	0–60°
[79]	VO_2	3	3.09–4.61 THz and 5.36–5.79 THz	1.95 THz	Over 90%	0–50°
This work	VO_2–Graphene	3	2.25–6.07 THz	3.82 THz	97.06%	0–60°

4. Conclusions

In this study, a dynamically tunable terahertz ultra-wideband phase change absorber based on a VO_2–graphene hybrid metasurface was successfully designed, and the dual functions of ultra-wideband absorption and efficient transmission were realized through VO_2 phase change. At 345 K (metallic state), the device exhibits an average excellent absorption performance of 97.06% in the range of 2.25–6.07 THz (bandwidth 3.82 THz). At 318 K (insulated state), it can not only maintain 3.6–5.08 THz broadband absorption, with an average absorption rate of 81.99%, but also achieves high transmittance of 67.66–69.51% in the 0.1–2.14 THz and 7.51–1 Hz frequency bands. Through the synergistic control of

phase change materials and two-dimensional materials, the design uses patterned graphene to simplify the preparation process, which has both polarization insensitivity and wide incidence angle stability. The physical mechanism of ultra-wideband absorption is revealed by impedance matching theory and surface E-field distribution analysis, and the tunability of the device is verified by a systematic study of Fermi level, relaxation time, and structural parameters. It is believed that this research will lay a foundation for the optimal design of related devices in the future and will provide new technical ideas for the development of terahertz switching, stealth technology, and sensing applications.

Author Contributions: Conceptualization, K.C., Z.W., M.G. and Z.Y.; data curation, K.C., Z.W., M.G. and H.M.; formal analysis, K.C., Z.W. and M.G.; methodology, K.C., Z.W., M.G. and Z.Y.; resources, K.C., Z.W. and M.G.; software, K.C., Z.W., M.G., Z.Y. and H.M.; data curation, K.C., Z.W., M.G., S.C., Z.Y. and B.L.; writing—original draft preparation, K.C., Z.W. and M.G.; writing—review and editing, K.C., Z.W., M.G., H.M. and Z.Y. All authors have read and agreed to the published version of the manuscript.

Funding: The authors are grateful for the support of the National Natural Science Foundation of China (No. 21506257).

Institutional Review Board Statement: Not applicable.

Informed Consent Statement: Not applicable.

Data Availability Statement: Publicly available datasets were analyzed in this study. The data can be found here: [https://www.lumerical.com/]. (accessed on 1 January 2020).

Conflicts of Interest: Author Kele Chen and Meizhang Guan are employed by the company Sichuan Intronics Electronic Technology Co., Ltd. The remaining authors declare that the research was conducted in the absence of any commercial or financial relationships that could be construed as a potential conflict of interest.

References

1. Yang, Q.; Yu, M.; Chen, Z.; Ai, S.; Kentsch, U.; Zhou, S.; Jia, Y.; Chen, F.; Liu, H. A novel approach towards robust construction of physical colors on lithium niobate crystal. *Opto-Electron. Adv.* **2025**, *8*, 240193. [CrossRef]
2. Balashov, I.S.; Chezhegov, A.A.; Chizhov, A.S.; Grunin, A.A.; Anokhin, K.V.; Fedyanin, A.A. Light-stimulated adaptive artificial synapse based on nanocrystalline metal-oxide film. *Opto-Electron. Sci.* **2023**, *2*, 230016. [CrossRef]
3. Zhao, J.; Lai, H.R.; Li, M. Anchoring 1T-MoS2 petals on N-doped reduced graphene oxide for exceptional electromagnetic wave absorption. *Int. J. Miner. Metall. Mater.* **2025**, *32*, 619–630. [CrossRef]
4. Wang, X.Y.; Lin, Q.; Wang, L.L.; Liu, G.D. Dynamic control of polarization conversion based on borophene nanostructures in optical communication bands. *Phys. Scr.* **2024**, *99*, 085531. [CrossRef]
5. Li, Y.C.; Chen, F. Tunable plasmon-induced transparency for advanced sensing in MoS2 based metamaterial. *Phys. Lett. A* **2025**, *553*, 130689. [CrossRef]
6. Xiao, T.X.; Tu, S.; Liang, S.Z.; Guo, R.J.; Tian, T.; Müller-Buschbaum, P. Solar cell-based hybrid energy harvesters towards sustainability. *Opto-Electron. Sci.* **2023**, *2*, 230011. [CrossRef]
7. Yang, C.; Luo, M.H.; Ju, X.W.; Hu, J.Y. Ultra-narrow dual-band perfect absorber based on double-slotted silicon nanodisk arrays. *J. Phys. D Appl. Phys.* **2024**, *57*, 345104. [CrossRef]
8. Zhang, J.; Chen, Y.; Chen, S.; Hou, J.; Liu, J. A simple ultra-broadband metamaterial solar perfect absorber with highly efficient photothermal conversion performance. *Phys. B Condens. Matter* **2025**, *699*, 416845. [CrossRef]
9. Yu, Z.; Li, M.; Xing, Z.; Gao, H.; Liu, Z.; Pu, S.; Mao, H.; Cai, H.; Ma, Q.; Ren, W.; et al. Genetic algorithm assisted meta-atom design for high-performance metasurface optics. *Opto-Electron. Sci.* **2024**, *3*, 240016. [CrossRef]
10. Wang, X.Y.; Huang, S.L.; Chen, Y.; Chen, S.J.; Dai, W.; Hou, J.; Wang, J.Y.; Yang, W.M.; Song, S.Y. Perfect absorber based on toroidal dipole in metamaterial of silicon and gallium phosphide. *Photonics Nanostruct. Fundam. Appl.* **2025**, *66*, 101410. [CrossRef]
11. Li, Y.M.; Tan, C.X.; Hu, J.Y.; Bai, W.D.; Zhang, R.L.; Lin, Q.; Zhang, Y.; Wang, L.L. Ultra-narrow band perfect absorbance induced by magnetic lattice resonances in dielectric dimer metamaterials. *Results Phys.* **2022**, *39*, 105730. [CrossRef]
12. Wang, Z.; Pan, W.K.; He, Y.; Zhu, Z.; Jin, X.; Liu, M.; Ma, S.; He, Q.; Sun, S.; Zhou, L.; et al. Efficient generation of vectorial terahertz beams using surface-wave excited metasurfaces. *Opto-Electron. Sci.* **2025**, *4*, 240024. [CrossRef]

13. Liu, Y.; Ma, X.; Chao, K.; Sun, F.; Chen, Z.; Shan, J.; Chen, H.; Zhao, G.; Chen, S. Simultaneously Realizing Thermal and Electromagnetic Cloaking by Multi-Physical Null Medium. *Opto-Electron. Sci* **2024**, *3*, 230027. [CrossRef]
14. Huffman, T.J.; Xu, P.; Qazilbash, M.M.; Walter, E.J.; Krakauer, H.; Wei, J.; Cobden, D.H.; Bechtel, H.A.; Martin, M.C.; Carr, G.L.; et al. Anisotropic Infrared Response of Vanadium Dioxide Microcrystals. *Phys. Rev. B* **2013**, *87*, 115121. [CrossRef]
15. Qazilbash, M.M.; Brehm, M.; Chae, B.-G.; Ho, P.-C.; Andreev, G.O.; Kim, B.-J.; Yun, S.J.; Balatsky, A.V.; Maple, M.B.; Keilmann, F.; et al. Mott Transition in VO_2 Revealed by Infrared Spectroscopy and Nano-Imaging. *Science* **2007**, *318*, 1750–1753. [CrossRef]
16. Yang, C.; Lin, Q.; Du, W.J.; Wang, L.L.; Liu, G.D. Bi-tunable absorber based on borophene and VO_2 in the optical telecommunication band. *J. Opt. Soc. Am. B* **2022**, *39*, 2969–2974. [CrossRef]
17. Li, W.X.; Cheng, S.B.; Yi, Z.; Zhang, H.F.; Song, Q.J.; Hao, Z.Q.; Sun, T.Y.; Wu, P.H.; Zeng, Q.D.; Raza, R. Advanced optical reinforcement materials based on three-dimensional four-way weaving structure and metasurface technology. *Appl. Phys. Lett.* **2025**, *126*, 033503. [CrossRef]
18. Ai, Z.; Yang, H.; Liu, M.S.; Cheng, S.B.; Wang, J.Q.; Tang, C.J.; Gao, F.; Li, B.X. Phase-Transition-Enabled Dual-Band Camouflage in VO2/Ag Multilayered Nanostructures. *Phys. E Low-Dimens. Syst. Nanostruct.* **2025**, *173*, 116327. [CrossRef]
19. Zhang, X.; Wang, G.; Liu, J.; Zuo, S.; Li, M.; Yang, S.; Jia, Y.; Gao, Y. Switchable and Tunable Terahertz Metamaterial Based on Vanadium Dioxide and Photosensitive Silicon. *Nanomaterials* **2023**, *13*, 2144. [CrossRef] [PubMed]
20. Kats, M.A.; Sharma, D.; Lin, J.; Genevet, P.; Blanchard, R.; Yang, Z.; Qazilbash, M.M.; Basov, D.N.; Ramanathan, S.; Capasso, F. Ultra-thin perfect absorber employing a tunable phase change material. *Appl. Phys. Lett.* **2012**, *101*, 221101. [CrossRef]
21. Driscoll, T.; Palit, S.; Qazilbash, M.M.; Brehm, M.; Keilmann, F.; Chae, B.G.; Yun, S.J.; Kim, H.T.; Cho, S.Y.; Jokerst, N.M.; et al. Dynamic tuning of an infrared hybrid-metamaterial resonance using vanadium dioxide. *Appl. Phys. Lett.* **2008**, *93*, 024101. [CrossRef]
22. Hu, J.Y.; Bai, W.D.; Tan, C.X.; Li, Y.M.; Lin, Q.; Wang, L.L. Highly electric field enhancement induced by anapole modes coupling in the hybrid dielectric-metal nanoantenna. *Opt. Commun.* **2022**, *511*, 127987. [CrossRef]
23. Jiang, B.; Hou, Y.; Wu, J.; Ma, Y.; Gan, X.; Zhao, J. In-fiber photoelectric device based on graphene-coated tilted fiber grating. *Opto-Electron. Sci.* **2023**, *2*, 230012. [CrossRef]
24. Wang, H.Y.; Ma, R.; Liu, G.D.; Wang, L.L.; Lin, Q. Optical force conversion and conveyor belt effect with coupled graphene plasmon waveguide modes. *Opt. Express* **2023**, *31*, 32422. [CrossRef]
25. Zeng, T.Y.; Liu, G.D.; Wang, L.L.; Lin, Q. Light-matter interactions enhanced by quasi-bound states in the continuum in a graphene-dielectric metasurface. *Opt. Express* **2021**, *29*, 40177–40186. [CrossRef]
26. Shao, M.R.; Ji, C.; Tan, J.B.; Du, B.Q.; Zhao, X.F.; Yu, J.; Man, B.; Xu, K.; Zhang, C.; Li, Z. Ferroelectrically modulate the Fermi level of graphene ox-ide to enhance SERS response. *Opto-Electron. Adv.* **2023**, *6*, 230094. [CrossRef]
27. Wang, P.; Yang, M.; Tang, S.; Li, Y.; Lin, X.; Zhang, H.; Zhu, Z.; Chen, F. Z-scheme heterojunctions composed of 3D graphene aerogel/g-C3N4 nanosheets/porous ZnO nanospheres for the efficient photocatalytic reduction of CO_2 with H_2O under visible light irradiation. *J. Alloys Compd.* **2022**, *918*, 165607. [CrossRef]
28. Li, W.; Yi, Y.; Yang, H.; Cheng, S.; Yang, W.X.; Zhang, H.; Yi, Z.; Yi, Y.; Li, H. Active Tunable Terahertz Band-width Absorber Based on single layer Graphene. *Commun. Theor. Phys.* **2023**, *75*, 045503. [CrossRef]
29. Zeng, Y.; Ling, Z.X.; Liu, G.D.; Wang, L.L.; Lin, Q. Tunable plasmonically induced transparency with giant group delay in gain-assisted graphene metamaterials. *Opt. Express* **2022**, *30*, 455954. [CrossRef] [PubMed]
30. Shen, J.; Li, H.; Qiu, X.; Lu, J.; Wang, Y.; Jin, C. VO2-Graphene based four-state ultra-wideband terahertz metamaterial with switchable absorption, reflection, and transmission. *Micro Nanostruct.* **2025**, *203*, 208143. [CrossRef]
31. Li, Z.T.; Cheng, S.B.; Zhang, H.F.; Yang, W.X.; Yi, Z.; Yi, Y.G.; Wang, J.Q.; Ahmad, S.; Raza, R. Ultrathin broadband terahertz metamaterial based on single-layer nested patterned graphene. *Phys. Lett. A* **2025**, *534*, 130262. [CrossRef]
32. Chen, Z.Y.; Cheng, S.B.; Zhang, H.F.; Yi, Z.; Tang, B.; Chen, J.; Zhang, J.G.; Tang, C.J. Ultra wideband absorption absorber based on Dirac semimetallic and graphene metamaterials. *Phys. Lett. A* **2024**, *517*, 129675. [CrossRef]
33. Kitamura, R.; Pilon, L.; Jonasz, M. Optical constants of silica glass from extreme ultraviolet to far infrared at near room tem-perature. *Appl. Opt.* **2007**, *46*, 8118–8133. [CrossRef] [PubMed]
34. Chen, S.; Wu, X.H.; Fu, C.J. Active tuning of anisotropic phonon polaritons in natural van der Waals crystals with negative permittivity substrates and its application in energy transport. *Opto-Electron. Sci.* **2024**, *3*, 240002. [CrossRef]
35. Ren, J.L.; Ma, Q.F.; Sun, X.F.; Ma, J.Y.; Liu, G.R.; Yang, H. In^{3+}-doping and oxygen vacancies co-engineering active sites of Bi_2WO_6 hollow nanospheres to achieve efficient photoreduction of CO_2 to CO with nearly 100% selectivity. *Fuel* **2025**, *397*, 135454. [CrossRef]
36. Zeng, Z.L.; Liu, H.F.; Zhang, H.F.; Cheng, S.B.; Yi, Y.G.; Yi, Z.; Wang, J.Q.; Zhang, J.G. Tunable ultra-sensitive four-band terahertz sensors based on Dirac semimetals. *Photonics Nanostruct. Fundam. Appl.* **2025**, *63*, 101347. [CrossRef]
37. Dai, Y.Y.; Liu, G.R.; Sun, X.F.; Ma, J.Y.; Xian, T.; Yang, H. Mn doping and ZnS nanoparticles modification on Bi_2MoO_6 to achieve an highly-efficient photocatalyst for TC degradation. *Appl. Surf. Sci.* **2025**, *681*, 161611. [CrossRef]

38. Yang, J.Q.; Lin, Q.; Wang, L.L.; Liu, G.D. Research of bound states in the continuum and their polarization control in dielectric metamaterial. *Phys. Scr.* **2025**, *100*, 065551. [CrossRef]
39. Luo, M.H.; Hu, J.Y.; Li, Y.M.; Bai, W.D.; Zhang, R.L.; Lin, Q.; Wang, L.L. Anapole-assisted ultra-narrow-band lattice resonance in slotted silicon nanodisk arrays. *J. Phys. D Appl. Phys.* **2023**, *56*, 375102. [CrossRef]
40. Liu, G.R.; Dai, Y.Y.; Sun, X.F.; Ma, J.Y.; Xian, T.; Yang, H. Synergistically regulating energy band structure and forming quantum wells to enhance the photocatalytic activity of Bi_2MoO_6 for tetracycline removal. *Sep. Purif. Technol.* **2025**, *361*, 131622. [CrossRef]
41. Hu, H.; Chen, F.; Li, Y.; Li, J.; Cui, L.; Jiang, D.; Lin, X.; Gao, J. Construction of graphene supported TiO_2 nanosheet array/CdS/Ni_2P composite with dual heterojunctions for boosting photocatalytic hydrogen evolution. *J. Alloys Compd.* **2025**, *1024*, 180216. [CrossRef]
42. Liu, S.H.; Chen, F. Dynamically tunable Fano resonance effect based on monolayer graphene with disk defect robustness. *Phys. B Condens. Matter* **2025**, *715*, 417638. [CrossRef]
43. Hu, J.Y.; Tan, C.X.; Bai, W.D.; Li, Y.M.; Lin, Q.; Wang, L.L. Dielectric nanocavity-coupled surface lattice resonances for high-efficiency plasmonic sensing. *J. Phys. D Appl. Phys.* **2022**, *55*, 075105. [CrossRef]
44. Qazilbash, M.M.; Li, Z.; Podzorov, V.; Brehm, M.; Keilmann, F.; Chae, B.; Kim, H.-T.; Basov, D. Electrostatic modification of infrared response in gated structures based on VO_2. Appl. *Phys. Lett.* **2008**, *92*, 24. [CrossRef]
45. Xiang, T.; Sun, Z.; Wang, L.L.; Lin, Q.; Liu, G.D. Polarization independent perfect absorption of borophene metamaterials operating in the communication band. *Phys. Scr.* **2024**, *99*, 085519. [CrossRef]
46. Huang, Z.; Liu, G.D.; Wang, L. Active modulation of quasi-bound state in the continuum based on bulk Dirac semimetals metamaterial. *Appl. Phys. Express* **2022**, *15*, 032006. [CrossRef]
47. Zhang, B.W.; Luo, Y.N. Dynamic optical tuning and sensing in L-shaped dirac semimetal-based terahertz metasurfaces. *Phys. Lett. A* **2025**, *541*, 130419. [CrossRef]
48. Liu, Y.J.; Liu, M.S.; Yang, H.; Yi, Z.; Zhang, H.; Tang, C.J.; Deng, J.; Wang, J.Q.; Li, B.X. Photoelectric simulation of perovskite solar cells based on two inverted pyramid structures. *Phys. Lett. A* **2025**, *552*, 130653. [CrossRef]
49. Gu, X.; Liu, X.; Yan, X.F.; Du, W.J.; Lin, Q.; Wang, L.L.; Liu, G.D. Polaritonic coherent perfect absorption based on self-hybridization of a quasi-bound state in the continuum and exciton. *Opt. Express* **2023**, *31*, 4691–4700. [CrossRef]
50. Liu, B.W.; Chen, F. Adjustable slow light and optical switch in a black phosphorus metamaterial based on double plasmon-induced transparency. *Phys. B Condens. Matter* **2025**, *714*, 417423. [CrossRef]
51. Ma, R.; Zhang, L.; Liu, G.; Wang, L.; Lin, Q. The total optical force exerted on black phosphorus coated dielectric cylinder pairs enhanced by localized surface plasmon. *J. Appl. Phys.* **2021**, *130*, 113103. [CrossRef]
52. Li, W.; Cheng, S.; Zhang, H.; Yi, Z.; Tang, B.; Ma, C.; Wu, P.; Zeng, Q.; Raza, R. Multi-functional metasurface: Ultra-wideband/multi-band absorption switching by adjusting guided mode resonance and local surface plasmon resonance effects. *Commun. Theor. Phys.* **2024**, *76*, 065701. [CrossRef]
53. Long, T.; Zhang, L.; Wang, L.L.; Lin, Q. Tunable narrow transparency windows induced by the coupled quasi-guided modes in borophene plasmonic nanostructure. *J. Phys. D Appl. Phys.* **2022**, *55*, 315101. [CrossRef]
54. Yan, X.F.; Lin, Q.; Wang, L.L.; Liu, G.D. Tunable strong plasmon–exciton coupling based modulator employing borophene and deep subwavelength perovskite grating. *J. Phys. D Appl. Phys.* **2023**, *56*, 435106. [CrossRef]
55. Cheng, S.B.; Li, W.X.; Zhang, H.F.; Akhtar, M.N.; Yi, Z.; Zeng, Q.D.; Ma, C.; Sun, T.Y.; Wu, P.H.; Ahmad, S. High sensitivity five band tunable metamaterial absorption device based on block like Dirac semimetals. *Opt. Commun.* **2024**, *569*, 130816. [CrossRef]
56. Yuan, Y.; Liu, H.F.; Liu, M.S.; Zhang, W.B.; Li, X.H.; Cheng, S.B. Design of wide-angle broadband titanium-nitride solar absorber based on column-cavity structure. *Phys. Lett. A* **2025**, *556*, 130832. [CrossRef]
57. Gu, X.; Liu, G.D.; Wang, L.L.; Lin, Q. Robust Fano resonance induced by topologically protected interface modes interference at gigahertz. *Appl. Phys. Express* **2022**, *15*, 082004. [CrossRef]
58. Li, L.Y.; Chen, F. Tunable four-band metamaterial absorber and sensor based on a stacking double-ring Dirac semimetal structure design. *Phys. Lett. A* **2025**, *544*, 130489. [CrossRef]
59. Li, Z.T.; Li, X.; Liu, G.D.; Wang, L.L.; Lin, Q. Analytical investigation of unidirectional reflectionless phenomenon near the exceptional points in graphene plasmonic system. *Opt. Express* **2023**, *31*, 30458. [CrossRef] [PubMed]
60. Ai, Z.; Liu, H.F.; Cheng, S.B.; Zhang, H.F.; Yi, Z.; Zeng, Q.D.; Wu, P.H.; Zhang, J.G.; Tang, C.J.; Hao, Z.Q. Four peak and high angle tilted insensitive surface plasmon resonance graphene absorber based on circular etching square window. *J. Phys. D Appl. Phys.* **2025**, *58*, 185305. [CrossRef]
61. Li, X.; Li, Z.T.; Wang, L.L.; Lin, Q. Unidirectional reflectionless propagation in borophene plasmonic metamaterials. *J. Phys. D Appl. Phys.* **2023**, *57*, 015103. [CrossRef]
62. Ren, J.L.; Ma, Q.F.; Sun, X.F.; Wang, S.F.; Liu, G.R.; Yang, H. Interface-engineering enhanced photocatalytic conversion of CO_2 into solar fuels over S-type Co-Bi_2WO_6@Ce-MOF heterostructured photocatalysts. *J. Colloid Interf. Sci.* **2025**, *691*, 137452. [CrossRef]
63. Ma, Q.; Ren, J.; Sun, X.; Wang, S.; Chen, X.; Liu, G.; Yang, H. Enhanced CO_2 photoreduction over S-scheme Sdoped-BiVO4/AgCl heterostructures and interface interaction mediated selective generation of CH_4. *Chem. Eng. J.* **2025**, *509*, 161444. [CrossRef]

64. Zhao, J.; Lu, Y.X.; Zhou, Z. Correlation filters based on temporal regularization and background awareness. *Comput. Electr. Eng.* **2020**, *86*, 106757. [CrossRef]
65. Sun, X.; Zhang, J.; Luo, M.; Ma, J.; Xian, T.; Liu, G.; Yang, H. Elevating photocatalytic H2 evolution over ZnIn2S4@Au@Cd0.7Zn0.3S multilayer nanotubes via Au-mediating H–S antibonding-orbital occupancy. *Chem. Eng. J.* **2024**, *499*, 156455. [CrossRef]
66. Chen, Y.; Song, S.Y.; Zhou, Z.K.; Chen, S.J.; Hou, J.; Yang, W.X. Multidielectric-metal laminated solar perfect absorber with ultra-high manufacturing error tolerance. *Phys. Scr.* **2025**, *100*, 065538. [CrossRef]
67. Ning, X.; Sun, T.Y.; Song, Q.J.; Yi, Z.; Cheng, S.B.; Wang, J.Q.; Zeng, Q.D.; Yi, Y.G. A modulated broadband polarimetric insensitive metamaterial absorber based on a monolayer of graphene. *Commun. Theor. Phys.* **2025**, *77*, 095702. [CrossRef]
68. Zhou, Z.; Xue, B.; Wang, H.; Zhao, J. Bidirectional multi-scale deformable attention for video super-resolution. *Multimed. Tools Appl.* **2024**, *83*, 27809–27830. [CrossRef]
69. Li, Z.; Song, Q.J.; Jia, L.B.; Yi, Z.; Cheng, S.B.; Wang, J.Q.; Li, B.X. Actively tunable multi-frequency narrowband terahertz absorber using graphene metamaterials. *Opt. Commun.* **2025**, *583*, 131768. [CrossRef]
70. Han, H.; Zhao, J.; Zhai, W.; Xiong, Z.H.; Niyato, D.; Renzo, M.D.; Pham, Q.V.; Lu, W.; Lam, K.Y. Reconfigurable Intelligent Surface Aided Power Control for Physical-Layer Broadcasting. *IEEE Trans. Commun.* **2021**, *69*, 7821–7836. [CrossRef]
71. Jiang, X.W.; Yan, T.H.; Zhu, J.J.; He, B.; Li, W.H.; Du, H.P.; Sun, S.S. Densely Connected Deep Extreme Learning Machine Algorithm. *Cogn. Comput.* **2020**, *12*, 979–990. [CrossRef]
72. Ma, Q.; Ren, J.; Sun, X.; Chen, X.; Liu, G.; Wang, S.; Yang, H. Strong evidence for interface-field-induced photocarrier sepa-ration in new $AgFeO_2$-$BiVO_4$ heterostructures and their efficient photo-Fenton degradation of ciprofoxacin. *Appl. Surf. Sci.* **2024**, *679*, 161275. [CrossRef]
73. Huang, S.L.; Chen, Y.; Yu, C.C.; Chen, S.J.; Zhou, Z.K.; Liang, J.; Dai, W. Optimized metamaterial solar absorber with ultra-wideband, polarization-independent and large incident angle-insensitive. *Chin. J. Phys.* **2024**, *89*, 740–747. [CrossRef]
74. Sun, X.F.; Xian, T.; Sun, C.Y.; Zhang, J.Q.; Liu, G.R.; Yang, H. Enhancing CO_2 photoreduction on Au@CdZnS@MnO_2 hollow nanospheres via electron configuration modulation. *J. Mater. Sci. Technol.* **2025**, *228*, 256–268. [CrossRef]
75. Li, Y.C.; Chen, F.; Yang, W.X. A multifunctional bidirectional metamaterial perfect absorber for efficient narrowband and broadband absorption. *Opt. Commun.* **2025**, *586*, 131878. [CrossRef]
76. Cao, F.L.; Chen, B.J. New architecture of deep recursive convolution networks for super-resolution. *Knowl. Based Syst.* **2019**, *178*, 98–110. [CrossRef]
77. Zhang, K.; Dong, S.; Wu, X.; Yu, K.; Liu, Y. Graphene-based tunable broadband metamaterial absorber for terahertz waves. *Opt. Laser Technol.* **2025**, *180*, 111490. [CrossRef]
78. Dai, S.; Liao, S.Y.; Pan, J.R.; Zhang, H. Theoretical study on ultra-wideband absorption and tripling octave frequency linear to circular polarization conversion tunable metastructure based on vanadium dioxide. *Nanoscale* **2025**, *17*, 12673–12683. [CrossRef]
79. Valathuru, M.; Pardhasaradhi, P.; Prasad, N.; Madhav, B.T.P.; Das, S.; Soliman, N.F.; Ghzaoui, M.E. Design and Analysis of Dual-band Hexagon-shaped Polarization-insensitive Metamaterial Absorber using Vanadium dioxide (VO_2) for Terahertz Applications. *Plasmonics* **2025**, *20*, 4221–4240. [CrossRef]

Disclaimer/Publisher's Note: The statements, opinions and data contained in all publications are solely those of the individual author(s) and contributor(s) and not of MDPI and/or the editor(s). MDPI and/or the editor(s) disclaim responsibility for any injury to people or property resulting from any ideas, methods, instructions or products referred to in the content.